Inviscid simulations of expansion waves propagating into structured particle beds at low volume fractions

Goran Marjanovic,[*] Jason Hackl, Mrugesh Shringarpure,[†] Subramanian Annamalai,
Thomas L. Jackson, and S. Balachandar

Department of Mechanical and Aerospace Engineering, University of Florida,
Gainesville, Florida 32611, USA

Expansion waves propagating into particle beds are found in many manmade and natural applications. Rapid decompression of a highly pressurized powder bed or a volcanic eruption are two such examples. In this investigation, we perform fully resolved simulations of expansion waves propagating into particle beds of three different volume fractions using the discontinuous Galerkin spectral element method code, CMT-NEK. We validate state-of-the-art drag models for a particle in an unsteady compressible flow and show good agreement, particularly at lower volume fractions. We model the particle bed as a nozzle or area reduction and, using isentropic flow relations, predict the final pressure, temperature, and Mach number extremely well in each case.

I. INTRODUCTION

Many engineering systems and natural phenomena occur in the compressible multiphase flow regime and therefore there is great value in studying and understanding fundamental properties of these flows. Red supergiants collapsing to supernovae or volcanic detonations sending out plumes of dust and debris are two such events observed in nature. The explosive dispersal of particles by the release of a pressurized multiphase canister is an example one might find in an engineering system. Nevertheless, whether it be the volcanic detonation or the pressurized canister release, these flows share several compressible flow features; the initial detonation that follows after the rupture of a diaphragm or a barrier will send out a shock wave followed by a contact interface, both of which propagate outward in the normal direction into the initial low-pressure region. Further, an expansion wave (also known as a rarefaction wave) is created and it propagates in the opposite direction into the high-pressure region, often interacting with particles. Potential applications of these types of flows include high-speed flow through porous media [1] and depressurization of fine powder beds [2].

In the context of multiphase flow, one can identify two different classes of scenarios. When particles are initially on the low-pressure side, they will be subjected to the outward propagating shock followed by the contact interface, upon the breaking of the diaphragm. An example of this type will be a smoke grenade, where a cylindrical explosive charge is surrounded by an annular bed of fine particles and flakes. Following the detonation of the explosive, an intense shock followed by a contact rapidly moves out and propels the particles in the radial direction, causing them to disperse. In contrast, if particles are located initially on the high-pressure side, they will experience the expansion wave once the diaphragm breaks. In the volcanic eruption case, the expansion wave

---

[*]gmarjanovic@ufl.edu

[†]Present address: ExxonMobil Upstream Research Company, Spring, TX 77389, USA.

propagates down into bed of debris, particles, and molten lava, causing it to spew back out. In fact, in any kind of pressurized particle or droplet-laden canister, as the expansion wave moves through the multiphase media, this behavior can be observed.

The canonical problem of a planar shock wave interacting with particles has been studied quite extensively. At the level of a single particle, its interaction with a shock wave has been studied experimentally and computationally by Igra and Takayama [3], Britan *et al.* [4], Tanno *et al.* [5], Sun *et al.* [6], Martinez *et al.* [7], and Bordoloi *et al.* [8]. The primary focus has been to calculate the complex nonmonotonic time-dependent drag on a single particle under shockwave loading. On the theoretical front, by solving the linearized compressible Navier-Stokes equations, Parmar *et al.* [9] developed an analytical model that predicted the drag on a single particle and compared the prediction to experimental and computational results to demonstrate its accuracy (Sun *et al.* [6]). The problem of shock interaction with an array (or a layer of) particles has also been studied to some depth. For example, Collins *et al.* [10] studied shock propagation in deuterium-tritium saturated foam. Lu *et al.* [11] simulated a shock interacting with a cloud of two-dimensional particles using direct numerical simulations along with an artificial neural network model for the prediction of forces on the particles. Hosseinzadeh-Nik *et al.* [12] studied shock-particle cloud interaction using particle-resolved direct numerical simulation, focusing on the flow unsteadiness and instabilities produced as a result of the shock wave. They showed that the kinetic energy in the fluctuating field is of the same order as in the mean flow field and therefore the Reynolds stress terms are too significant to neglect when modeling these types of flows. Regele *et al.* [13] performed two-dimensional simulations of shock interacting with cylinders. Sridharan *et al.* [14] considered axisymmetric inviscid simulations and Mehta *et al.* [15–17] considered three-dimensional inviscid simulations of a planar shock propagation through structured and random arrays of particles. They observed that although the initial peak force on each particle depended mainly on its interaction with the primary shock propagating through the array, subsequent force history strongly depended on the compression and rarefaction waves that diffract off the neighboring particles. Thus, current theoretical force models, which are based on an isolated particle, are insufficient to characterize this later time force evolution that is dominated by interaction between the particles. The effect of shock propagation over a curtain of particles has been studied experimentally and computationally by Wagner *et al.* [18,19], Ling *et al.* [20], Theofanous *et al.* [21], McFarland *et al.* [22], and DeMauro *et al.* [23], where the focus has been on the downstream spreading of the curtain.

In comparison, the other canonical limit of an expansion wave interacting with particles has not been studied to the same length. At the level of a single particle, Annamalai and Balachandar [24] advanced the theoretical unsteady drag force model in a compressible flow of Parmar *et al.* [9] and tested it against direct numerical simulation of an expansion wave propagating over an isolated particle to demonstrate very good agreement. The problem of a bed of particles being subjected to an expansion wave is most relevant to volcanic eruption, which can be modeled as a cavity of gas-particle mixture under very high pressure being suddenly released to the ambient. Cagnoli *et al.* [2] performed experiments of depressurization of fine powders and more recently similar experiments with a bed of particles in the high-pressure region of a shock tube have been considered by Chojnicki *et al.* [25] and Cigala *et al.* [26]. By placing the particles on the high-pressure side of the shock tube, after the bursting of the diaphragm, an expansion wave sweeps over the particles. Attention was focused on the propagation of the particle front as well as the nature of instabilities that led to the formation of void within the expanding bed of particles. An expansion wave provides an interesting contrast to a shock wave. In a shock wave, the physical quantities themselves jump across the shock wave, which remains relatively sharp. An expansion wave has an interesting feature that the physical properties vary continuously across it without any discontinuities. However, there are two sharp discontinuities in the first derivatives of the physical quantities at the head and the tail of the wave. Both the head and the tail of the expansion wave move at the local speed of sound in the frame attached to the local gas. In the case of the head of the expansion wave, since it moves into the static high-pressure section, the velocity of the head, in the laboratory frame of reference,

is the local speed of sound, and ahead of the head the gas properties are constant at their *prehead* values. The behavior of the tail of the expansion wave depends on the pressure ratio. At small pressure ratios, the tail also propagates into the initial high-pressure section at a velocity slower than the head and the gas velocity at the tail of the expansion remains subsonic. For this subcritical expansion wave, the laboratory frame velocity of the tail will be the local speed of sound minus the local subsonic gas velocity. At a specific pressure ratio, the gas velocity at the tail will be just sonic and correspondingly the velocity of the tail of the expansion wave will be identically zero in the laboratory frame of reference. Thus, in the case of a critical expansion wave, the tail will be located at the diaphragm. At higher pressure ratios, the tail propagates out into the low-pressure section and the gas velocity at the tail is supersonic. The region between the head and tail defines the expansion wave and the gas properties (such as pressure, density, and velocity) monotonically vary across the expansion wave from their prehead value to their *post-tail* value, and beyond the tail the flow remains uniform at the post-tail values. Since the head and tail of the expansion wave move at different velocities, the expansion wave broadens over time.

In a multiphase shock tube with particles in the high-pressure section, after the rupture of the diaphragm, the head and tail of the expansion wave begin to travel immediately upstream. Before the arrival of the head of the expansion wave, the particles in the high-pressure region experience no flow. As seen by a particle, the gas velocity passing over it increases continuously and reaches a constant value (uniform flow) after the passage of the tail of the expansion wave. If the particle is frozen in position as in a porous medium, the final gas velocity will be the post-tail gas velocity in the case of a subcritical expansion wave, or will approach the sonic velocity in the case of critical or supercritical expansion. In the case of a particle free to move, the particle will accelerate, enter into the initial low-pressure section, and eventually propagate out of the expansion into the post-tail constant region. For a particle initially located close to the diaphragm, the head of the expansion wave will arrive immediately after the breakage of the diaphragm and the change from pre-head to post-tail condition happens very rapidly. Deeper inside the particle bed, i.e., away from the diaphragm, it takes a progressively longer time for the head and tail to arrive and to pass.

In this study, we focus on an expansion wave moving into a stationary particle bed. By keeping the particles stationary, the present study is closer to an expansion wave moving through porous media. In addition, we will study this problem in the inviscid limit because we want to examine the unsteady inviscid effects experienced at early times by the particles. We isolate this problem away from turbulent effects by examining it in the inviscid limit. In this way, we can look at purely the effects of compressibility before building up to a more physically complex and more computationally costly problem.

Mehta *et al.* [16] examined various important timescales in a shock-particle interaction problem and a similar analysis will be considered for an expansion fan. The inviscid timescale can be defined as $\tau_i = d/u_r$, where d is the particle diameter and u_r is the relative velocity between the particle and the surrounding flow. As the head of the expansion moves past a stationary particle, initially the relative velocity starts at small values and correspondingly the inviscid timescale is large. As the tail of the expansion fan sweeps past the particle, the relative velocity reaches its largest value, whose magnitude is determined by the strength of the expansion fan. In the present case to be considered, the Mach number of the post-tail flow is 0.6. The viscous timescale can be defined as $\tau_v = \delta^2/\nu$, where ν is the kinematic viscosity of the gas and $\delta = d/\sqrt{\mathrm{Re}_p}$ is the estimate of the viscous boundary layer thickness on the particle. Here the particle Reynolds number is given in terms of relative velocity as $\mathrm{Re}_p = u_r d/\nu$. It can readily be seen that the viscous timescale of boundary layer development is of the same order as the inviscid timescale. We can also evaluate the acoustic timescale of the problem as $\tau_a = d/c$, where c is the speed of sound. The acoustic timescale is much larger than the viscous and inviscid timescales at the beginning when the head of the expansion fan crosses the particle, but later when the tail interacts with the particle all the scales are of the same order. In any case, the viscous effects quickly become important when an expansion fan interacts with a bed of particles, but we will ignore this effect in this study to better isolate the effects of compressibility. We now evaluate the importance of particle motion and the assumption

of stationary particles. The timescale on which the particle accelerates and approaches the ambient velocity is given by $\rho d^2/(18\nu)$, where ρ is the particle-to-gas density ratio. For a particle located at a streamwise distance X inside the high-pressure region from the diaphragm, the arrival times of the expansion fan head and tail are given by X/c and $X/(cM_t)$, respectively, where M_t is the Mach number of the tail (which in the present simulations has been chosen to be 0.4). Thus, the time taken for the expansion fan to fully cross the particle depends on its location and is given by $X(1 - M_t)/(cM_t)$, whose scale can be taken to be $\mathcal{O}(X/c)$. This is the timescale on which the ambient flow velocity changes as the expansion fan sweeps past the particle. The ratio of particle timescale to this expansion fan timescale can be expressed as $\rho(\mathrm{Re}_p/18)(c/u_r)(d/X)$. We consider a heavy particle of $\rho \sim \mathcal{O}(10^3)$. We can also estimate the Reynolds number of a particle of size of the order of 100 microns to be more than $\mathcal{O}(10^2)$. Also, for a sufficiently strong expansion fan $(c/u_r) \sim \mathcal{O}(1)$. The value of the timescale ratio is then determined by the particle position. Here we will consider particles located sufficiently close to the diaphragm [i.e., $(d/X) \sim \mathcal{O}(1)$] that the timescale ratio is very large, which indicates that the particle motion during the time of interaction with the expansion fan is very small. However, in cases when $X > d$, the passage of the expansion fan over the particle may be sufficiently slow that particle motion during this interaction cannot be neglected.

An analytical force model for a particle subjected to unsteady compressible flows [9,24] takes the form of an integrodifferential equation. The two important features of the model are that (i) it accounts for the unsteady force contributions that play an important role as the expansion wave sweeps past the particle and (ii) it accounts for the fact that the flow could vary substantially on the scale of the particle. For example, when a shock propagates over a particle, since the shock is often much thinner than the particle, at times when the shock is located on the particle, part of the particle is in the preshock state while the rest is in the postshock state, making the definition of gas velocity seen by the particle ambiguous. The above model has been rigorously tested in the context of shock-particle interaction and shown to perform well. The expansion wave going over a structured array of particles provides another test because there is a rapid change in the gas velocity, pressure, and density as the wave is sweeping past. The goal of our work is to compare our fully resolved simulation results with the inviscid components of the model of Annamalai and Balachandar [24].

The theoretical model is for an isolated particle. Its application for the present case of a structured array of particles will be strictly valid only during the early stages when the head of the expansion wave moves over the particle. Soon, diffracted waves from neighboring particles will interfere and change the aerodynamic force on the particles. Researchers have examined and modeled compressible flows through discontinuous cross-sectional area changes [27–29]. Using a similar analysis, here we model the particle bed as a flow obstruction and sudden area reduction and compare our simulation results to the analytical solutions obtained from isentropic flow relations.

We begin Sec. II by describing our numerical technique and discussing other assumptions made in this study. In Sec. III, we will present our results and compare them to those expected from the aforementioned theoretical model. The final section, Sec. IV, will discuss the conclusions.

II. METHODOLOGY

The domain setup is that of a shock tube, shown in Fig. 1, with the area in red representing the actual computational domain of interest. A shock tube consists of a high-pressure side on the left and a low-pressure side on the right separated by a diaphragm. In our case, we have a high-pressure, high-temperature region on the left and a low-pressure, low-temperature region on the right, though the temperature discontinuity is not necessary in a shock tube. Upon bursting of the diaphragm, a shock wave forms and immediately propagates to the right side, followed by a contact interface, which separates the driver gas and driven gas. Immediately propagating to the left is the head of an expansion wave, followed by the tail, and then uniform flow thereafter. The problem of interest has an initial pressure ratio of 4.85. We then compute the initial conditions for an expansion wave
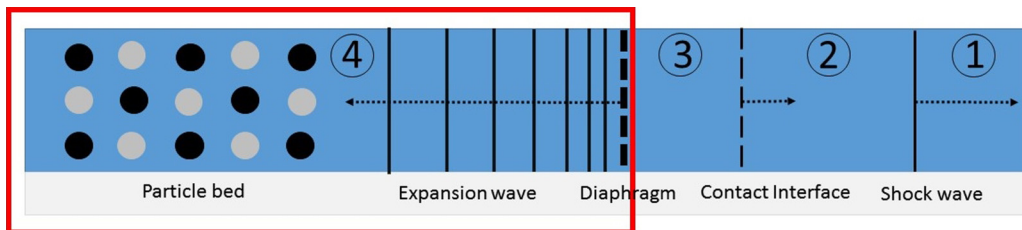
FIG. 1. Shock tube domain set up with the computational area of interest outlined in red. State 4 and state 1 are the driver section and the driven section respectively. When the diaphragm bursts, a shock wave and contact interface rapidly accelerate to the right while a series of expansion waves propagate toward the left, moving through a structured array of particles. State 2 represents the postshock state and state 3 represents the state between the contact interface and the expansion wave.

and simulate only the red area in Fig. 1. This can be done using a Riemann problem solver such as described by Toro [30]. This pressure ratio results in an expansion wave with a tail Mach number of 0.4 in the laboratory frame. The local gas travels at a subsonic Mach number of 0.6 in the opposite direction of the tail. The properties of the high-pressure prehead section and those of the post-tail constant section are shown in Table I.

The computational mesh is shown in Fig. 2, with the entire three-dimensional grid shown in Fig. 2(a), a face-centered cubic (fcc) unit cell in Fig. 2(b), and an inside view of the unit cell in Fig. 2(c), where the particles and the spectral element grid around them can be seen. Shown in Fig. 3 is a two-dimensional slice through the center (top frame) and lateral boundary (bottom frame) of the mesh for the computational domain, where the 21 layers of particles can be seen.

Particle layers 1, 2, and 3 represent one unit cell of an fcc arrangement, particle layers 3, 4, and 5 represent a second unit cell, and so on; hence there are 10 such unit cells with particles. Note that slip walls and thus geometric symmetry is employed along the two transverse directions. The unit cell is size $4 \times 4 \times 4$ in nondimensional units based on the particle diameter. The spheres comprising the FCC arrangements have been sized so as to give a desired average global volume fraction, ϕ. Here we consider three different simulations with particle volume fractions of 3.27%, 9.54%, and 15.15%, which correspond to particles of nondimensional sizes $d = 1.0$, 1.43, and 1.67 respectively. For simplicity, we will round the volume fractions to the nearest integer value and refer to the cases as $V3$, $V10$, and $V15$. Locally, the area fraction varies along the streamwise direction

TABLE I. Table of initial conditions and other relevant parameters for this study. P, T, and ρ are the pressure, temperature, and density of the gas. The ratio P_4/P_1 is the initial pressure ratio across the diaphragm of the shock tube used to generate an expansion wave with a tail Mach number, Ma_{tail}, of 0.4 in the laboratory reference frame.

Parameters	
P_4/P_1	4.85
P_3/P_4	0.651
T_3/T_4	0.884
ρ_3/ρ_4	0.68
Ma_{tail}	0.4

(a)

(b)   (c)
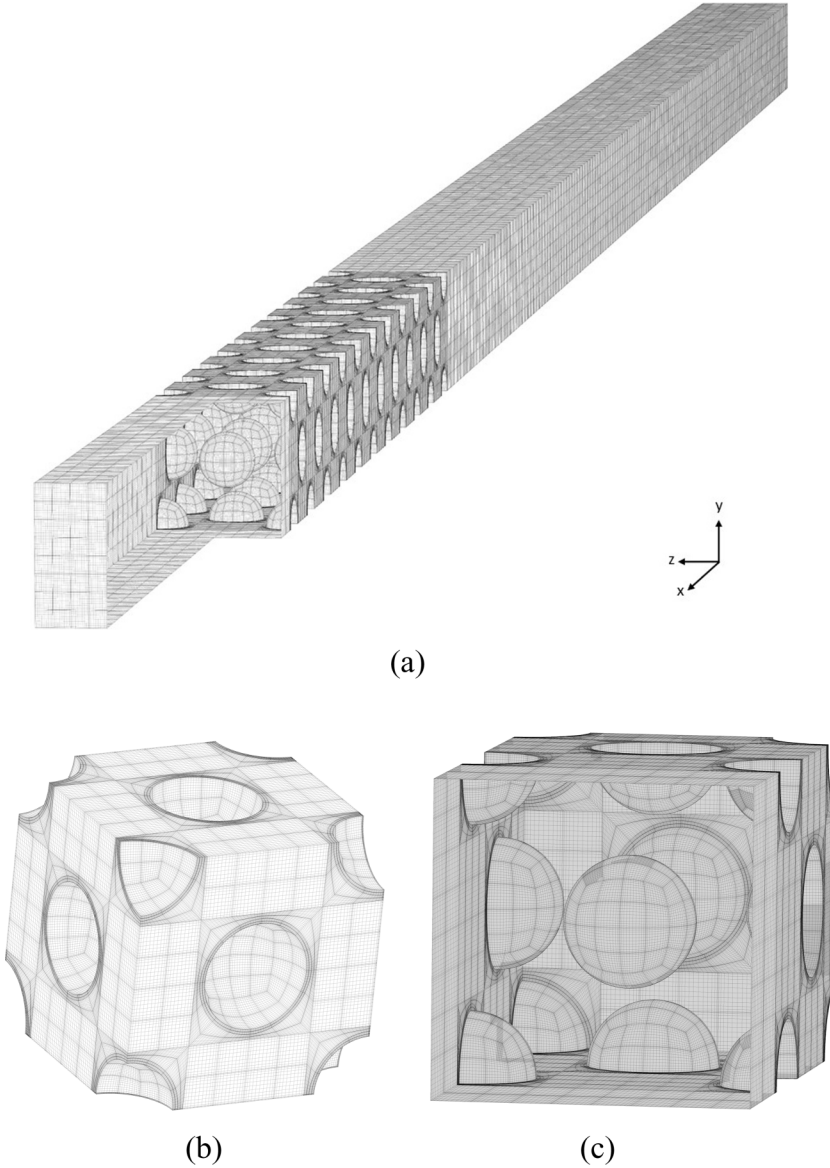
FIG. 2. Plotted here are (a) a three dimensional view of the simulation grid, (b) a representative face-centered cubic (FCC) unit cell, and (c) an inside view of the FCC unit cell.

and for the present fcc arrangement, averaged in y and z, can be expressed as

$$
\begin{cases}
\frac{\pi}{32}\left[\left(\frac{96\phi}{\pi}\right)^{2/3} - 4(x'+2n)^2\right] & \text{for } -2n - \left(\frac{12\phi}{\pi}\right)^{1/3} \leqslant x' \leqslant -2n + \left(\frac{12\phi}{\pi}\right)^{1/3} \\
& \text{where } n = 0, 1, 2, 3, \ldots, \\
0 & \text{otherwise.}
\end{cases}
\tag{1}
$$

The variable x' is directed backward from the center of the first layer of particles. At the center of each layer of particles (i.e., for $x' + 2n = 0$), the local area fraction is a maximum, whose value is $\frac{\pi}{32}\left(\frac{96\phi}{\pi}\right)^{2/3}$. Hence, for mean volume fractions of 3.27%, 9.54%, and 15.15%, local maximum area fractions are 9.81%, 20.04%, and 27.27%, respectively. Away from the centers,
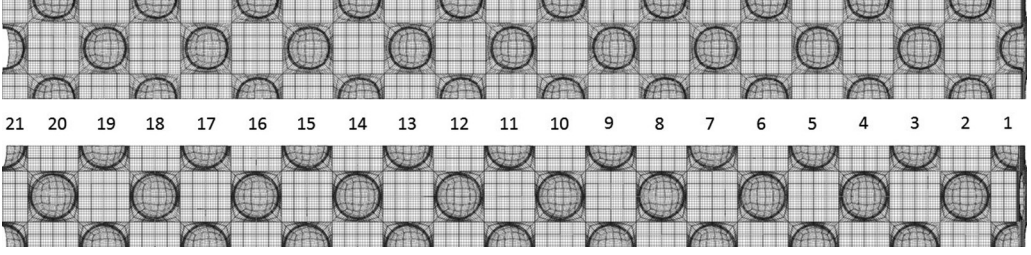
FIG. 3. Two-dimensional view of a centerline slice (top) and a wall slice (bottom) of the particle bed mesh. Each particle layer is labeled, starting with 1 on the far right and proceeding upstream to 21.

the area fraction decreases quadratically and becomes zero at $x' + 2n = \pm(\frac{12\phi}{\pi})^{1/3}$. The thickness of the region between the particles where the cross-sectional area fraction is zero is given by $2[1 - (\frac{12\phi}{\pi})^{1/3}]$, whose value for the three volume fractions are 1.0, 0.57, and 0.33, respectively. Only for $\phi > 26.18\%$ does the region of zero cross-sectional area fraction disappear. We will see later that this variation in area fraction will manifest itself as fluctuations in the mean quantities.

A. Euler equations of gas dynamics

In this section, we present the inviscid compressible flow governing equations being solved, with bold-faced quantities denoting vectors in $\mathbb{R}^3$ except for the conserved variables $\mathbf{U}$,

$$\mathbf{U} = [\rho, \rho u, \rho v, \rho w, \rho E]^\top, \tag{2}$$

which live in $\mathbb{R}^5$. The mth component of $\mathbf{U}$ is governed by the conservation law

$$\frac{\partial U_m}{\partial t} + \mathbf{\nabla} \cdot \mathbf{H}_m = 0, \quad m \in [1, 5]. \tag{3}$$

The gas velocity $\mathbf{u}$ is

$$\mathbf{u} = \begin{bmatrix} u \\ v \\ w \end{bmatrix} = \begin{bmatrix} u_1 \\ u_2 \\ u_3 \end{bmatrix}, \tag{4}$$

and ρ is the gas density, E is the mass-specific total energy $e + \frac{1}{2}|\mathbf{u}|^2$ of the gas, e is the gas internal energy, and p is the thermodynamic gas pressure.

$\mathbf{H}_m(\mathbf{U}) : \mathbb{R}^{5\times3} \to \mathbb{R}^3$ is the flux vector of equation m. For gas density, $\mathbf{H}_1(\mathbf{U})$ is

$$\mathbf{H}_1 = \rho\mathbf{u} = [U_2, U_3, U_4]^\top. \tag{5}$$

For gas momentum U_{2-4}, the convective fluxes are

$$\mathbf{H}_2 = \begin{bmatrix} (\rho u)u + p \\ (\rho u)v \\ (\rho u)w \end{bmatrix}, \tag{6}$$

$$\mathbf{H}_3 = \begin{bmatrix} (\rho v)u \\ (\rho v)v + p \\ (\rho v)w \end{bmatrix}, \tag{7}$$

$$\mathbf{H}_4 = \begin{bmatrix} (\rho w)u \\ (\rho w)v \\ (\rho w)w + p \end{bmatrix}, \tag{8}$$

and, for total energy ρE,

$$\mathbf{H}_5 = \mathbf{u}(\rho E + p). \tag{9}$$

The system is closed by an equation of state,

$$[p, T] = \text{EOS}(\rho, e). \tag{10}$$

Internal energy per unit mass $e = E - \frac{1}{2}|\mathbf{u}|^2$ is related to gas temperature T by the intensive property c_v, the constant-volume specific heat, such that

$$e = \int c_v(T)dT. \tag{11}$$

Generally, (11) must be solved for temperature T implicitly, iteratively, or via tabulation. While the method is only demonstrated for calorically perfect gases, it admits general equations of state provided the physical entropy is a concave function of the internal energy. For calorically perfect gases, c_v is constant. For both thermally and calorically perfect gases, pressure is obtained last via

$$p = \rho R T, \tag{12}$$

where the specific gas constant $R = (\gamma - 1)c_v$ requires the specification of $\gamma = c_p/c_v$, the ratio of constant-pressure specific heat c_p to c_v. Finally, the sound speed is

$$c = \sqrt{\frac{\gamma p}{\rho}} = \sqrt{\gamma R T}. \tag{13}$$

B. Numerical method

The simulations in this study were carried out with the code CMT-NEK. CMT-NEK uses the discontinuous Galerkin spectral element method (DGSEM) built on top of the NEK5000 [31] continuous spectral element method to extend it to compressible flows. DGSEM is a variational method; it is a particular form of the nodal discontinuous Galerkin method [32] using nested tensor products of Lagrange polynomials to approximate the unknown variables on deformed hexahedral elements. Discontinuities between the approximations of the unknowns at the shared faces of neighboring elements are treated as initial states to a Riemann solver which provides a "numerical flux" between elements in the surface integral that arises from integrating the flux divergence in the variational inner product by parts. Comprehensive descriptions and analysis of this approach may be found in textbooks [33, § 5.8] and in descriptions of its application to the compressible Navier-Stokes equations [34,35].

CMT-NEK solves the Euler equations (3)–(9) for the conserved unknowns in weak form [36] collocated on the $N \times N \times N$ Gauss-Lobatto-Legendre (GLL) quadrature nodes [37, appendices] in the $[-1, 1]^3$ reference element to which each element is isoparametrically mapped [38, § 4.4]. The nonlinear inviscid fluxes are dealiased [39] by interpolating the mesh transformation metrics, conserved variables, and primitive variables (like pressure and velocity) to $M = 3(N-1)/2$ Gauss-Legendre (GL) points in each direction of the reference element, evaluating equations (5)–(9) and the weak-form derivative operators on this fine grid, and projecting the volumetric fluxes back to the grid of N^3 GLL nodes. The numerical flux comes from the AUSM+ Riemann solver of Liou [40], and it too is evaluated on an M^2 grid on each face for dealiasing. The total-variation-diminishing third-order Runge-Kutta scheme [41] handles time marching. Further details, description, and validation are presented by Hackl *et al.* [42].

C. Grid resolution

We first carry out a grid resolution study for an isolated single particle at four different polynomial orders of $N = 6, 9, 12,$ and 18 and it is plotted in Fig. 4. A polynomial order of 6 is apparently too coarse and has undershoots in the drag profiles. As the polynomial order was
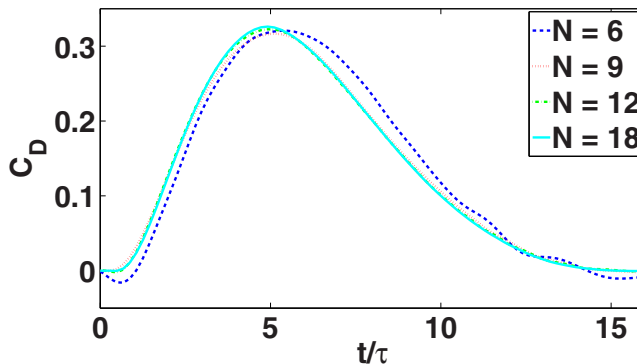
FIG. 4. Convergence study showing the drag coefficient for a single particle at four different polynomial orders.

increased, a converged profile was attained. Polynomial orders of 12 and 18 are nearly identical and for computational efficiency, 12 was selected for the present simulations.

D. Boundary conditions

Table I summarizes the detailed conditions used for the simulations. Each simulation used identical initial and boundary conditions with the only difference between the cases being the volume fraction. Each simulation used 29 568 spectral elements at a polynomial order $N = 12$ for all three spatial directions, resulting in 64 960 896 grid points. The domain has dimensions of $L_x \times L_y \times L_z$ equal to $126 \times 4 \times 4$. The particle bed consists of 95 particles fixed in space, arranged in a face-centered cubic structure. The particles are assumed to be much more massive than the surrounding gas and hence held stationary for this study. The following boundary conditions are employed for the computational domain shown in Fig. 2(a). On the upstream boundary (top right of image) of the computational domain, the fluid is stationary before the arrival of the head of the expansion wave and in the present simulations until the end of the computation the fluid at the upstream boundary remains stationary. Subsonic outflow boundary conditions are used at the downstream boundary [bottom left of Fig. 2(a)] of the computational domain. Because of the inviscid nature of the governing equations, no-penetration boundary conditions are adequate on the surface of the spheres. On the lateral surfaces of the computational domain slip wall boundary conditions are used (i.e., no penetration and no stress on their lateral boundaries). The implementation details of these boundary conditions in the context of DGSEM are discussed below. In the discontinuous Galerkin formalism, the same numerical flux functions used to couple elements together may be used to weakly enforce boundary conditions in two different ways: one for Dirichlet boundary conditions and the other for Neumann boundary conditions [43,44]. Dirichlet boundary conditions, meant to impose the solution directly at points lying on the boundary, appear in the numerical flux on element faces with Dirichlet boundary conditions done by replacing the state that would otherwise come from a neighboring element with the Dirichlet boundary condition $\mathbf{U}_D(\mathbf{U}^-)$, which can depend on the flow solution $\mathbf{U}^-$ at the quadrature nodes lying on the face of a boundary element $\partial \Omega_e$. Conversely, Neumann boundary conditions may often be imposed directly by substituting the desired flux for the numerical flux. At outflows, the state

$$
\mathbf{U}_D^{\text{out}} =
\begin{bmatrix}
\rho_o \\
\rho_o\, u_o \\
\rho_o\, v_o \\
\rho_o\, w_o \\
\rho_o \left(\frac{p_o}{(\gamma-1)\rho_o} + \frac{1}{2}|\mathbf{u}_o|^2 \right)
\end{bmatrix},
\tag{14}
$$

follows the procedure of Belk *et al.* [45], which states $p_o = p_\infty$, for some freestream pressure p_∞, and

$$\rho_o = \rho^- - \frac{p^- - p_\infty}{(a^-)^2}, \tag{15}$$

$$\mathbf{u}_o = \mathbf{u}^- + \frac{p^- - p_\infty}{\rho^- a^-}\hat{\mathbf{n}}. \tag{16}$$

Slip walls are enforced by solving the Riemann problem arising from the jump between the interior trace of the solution at the wall $\mathbf{U}^-$ and a "mirrored" state [44, § 8.3.1.2],

$$\mathbf{U}_D^{\text{wall}} = \begin{bmatrix} U_1^- \\ \rho^- u_{\text{ref}} \\ \rho^- v_{\text{ref}} \\ \rho^- w_{\text{ref}} \\ U_5^- \end{bmatrix}, \tag{17}$$

which is made up of the interior trace of the density and total energy fields at the boundary and the reflected velocity field $\mathbf{u}^{\text{ref}}$

$$\mathbf{u}^{\text{ref}} = \mathbf{u}^- - 2(\hat{\mathbf{n}} \cdot \mathbf{u}^-)\mathbf{u}. \tag{18}$$

III. RESULTS

A. Theoretical force model

Though the spheres in this study are stationary, it is important to obtain the drag forces acting on the particles from the fully resolved inviscid simulations and compare against the corresponding predictions from the model in order to evaluate the strengths and limitations of the model in accurately predicting the actual forces. Following Annamalai and Balachandar [24], the generalized Faxén (GF) form of the force expression will be used to predict the force on the spherical particle subjected to a time-dependent compressible flow. Since we are assuming to be in the inviscid limit, this equation reduces to the following form shown in Eq. (19). Here $R = d/2$ is the radius of the particle, and $\mathbf{u}^{un}$ and ρ^{un} are gas velocity and gas density at the particle location in the undisturbed state and therefore denoted by the superscript un. The force expression below, and for that matter all other force expressions, attempt to predict the force on the particle in terms of the undisturbed flow approaching the particle, where the term "undisturbed" denotes the flow that would exist in the absence of the particle under question but in the presence of all other particles. In the present context, the undisturbed ambient flow is the expansion wave, whose solution is known only in the limit of zero volume fraction. At finite volume fraction, the undisturbed flow approaching a particle is modified by the presence of all other particles. The theoretical results to be presented below ignore this effect of particles back on the flow and assume the undisturbed flow to be the planar expansion wave. As will be seen below, this results in the inability of the model to predict the long time evolution of the force:

$$\mathbf{F}(t) = \mathbf{F}_{pg}(t) + \mathbf{F}_{iu}(t) = \frac{4}{3}\pi R^3 \overline{\rho^{un}\frac{D\mathbf{u}^{un}}{Dt}}^V + 4\pi R^3 \int_{\tilde{\xi}=-\infty}^{\tilde{t}} K_{iu}(\tilde{t} - \tilde{\xi}; M)\left[\frac{D}{Dt}\overline{\rho^{un}\mathbf{u}_r^{un}}^S\right]_{\tilde{t}=\tilde{\xi}} d\tilde{\xi}. \tag{19}$$

The integrodifferential equation given in (19) includes only the two inviscid force contributions: the undisturbed flow force (or the pressure-gradient force) $\mathbf{F}_{pg}$ and the inviscid unsteady force (also known as the added-mass force in the incompressible limit) $\mathbf{F}_{iu}$. The more general force expression given in Annamalai and Balachandar [24] includes two other viscous contributions, namely the quasisteady force and the viscous unsteady force, which are ignored in the above expression because we will compare the theoretical predictions with the present simulations, which are conducted in the

inviscid limit. In the traditional application of the force formulas, gas properties such as density (ρ^{un}) and velocity ($\mathbf{u}^{un}$) are evaluated at the center of the particle. This simplified approach is adequate when the particle size is smaller than the scales of ambient flow variation. This is clearly not the case in the context of a shock or an expansion wave passing over a particle, since the gas properties vary substantially across the particle and the gas properties cannot be taken to be those at the particle center. The generalized Faxén form resolves this dilemma by defining the undisturbed gas properties in terms of averages over the volume and surface of the particle, which are denoted as $\overline{(.)}^V$ and $\overline{(.)}^S$, respectively.

The pressure gradient force [the first term on the right of Eq. (19)] is simply the force that an equivalent volume of fluid would experience in the absence of the particle, and in the present Euler flow it is strictly due to the pressure gradient (viscous stresses are zero). In this term, D/Dt represents the total derivative following the fluid and thus the first term corresponds to mass times acceleration of the undisturbed fluid that would occupy the particle volume. The inviscid unsteady force (the second term on the right) is the additional force required by the perturbation flow created due to the presence of the particle. In an inviscid flow, the perturbation flow must be such that, on the surface of the particle, the total flow must satisfy the no-penetration boundary condition. In other words, the perturbation flow on the surface of the particle must cancel the normal component of the undisturbed flow. This is the reason the second term depends only on the density-weighted radial component of the undisturbed flow velocity $\rho_0^{un}\mathbf{u}_r^{un}$ averaged over the surface of the particle. Note that $\mathbf{u}_r^{un} = (\mathbf{u}^{un} \cdot \mathbf{e}_n)\mathbf{e}_n$, where $\mathbf{e}_n$ is the unit vector along the outward normal direction to the particle.

The following alternate form of the inviscid unsteady force can be obtained by exploiting an analytic relation between the surface and volume averages (see Appendix C of Ref. [24]),

$$\mathbf{F}_{iu}(t) = \frac{4}{3}\pi R^3 \int_{\tilde{\xi}=-\infty}^{\tilde{t}} K_{iu}(\tilde{t}-\tilde{\xi}; M)\left[\overline{\frac{D}{Dt}\rho^{un}\mathbf{u}^{un}}^V + \overline{\frac{D}{Dt}\mathbf{r}\nabla\cdot(\rho^{un}\mathbf{u}^{un})}^V\right]_{\tilde{t}=\tilde{\xi}} d\tilde{\xi}, \qquad (20)$$

where $\mathbf{r}$ is the radial vector from the center of the particle. In the limit of nearly incompressible flow, ρ^{un} equals the constant fluid density and $\nabla \cdot \mathbf{u}^{un} \to 0$. In this limit, thus, the second term is negligible, while the first term becomes

$$m_f \int_{\tilde{\xi}=-\infty}^{\tilde{t}} K_{iu}(\tilde{t}-\tilde{\xi}; M)\left[\overline{\frac{D}{Dt}\mathbf{u}^{un}}^V\right]_{\tilde{t}=\tilde{\xi}} d\tilde{\xi}, \qquad (21)$$

where we have used the fact that the mass of the displaced fluid is given by $m_f = 4\pi R^3\rho/3$. Therefore, this term can be directly related to the added-mass force and the complete form given in Eq. (19) or (20) accounts for flow compressibility and density variation across the particle. Also Annamalai and Balachandar [24] used the definition $\overline{D/Dt} = \partial/\partial t + \overline{\mathbf{u}^{un}}^V \cdot \nabla$, where the second term on the right was added to account for the nonlinear effect due to convective acceleration. The rigorous derivation in the linear limit only yielded the temporal acceleration and Annamalai and Balachandar [24] showed that the inclusion of the empirical second term improved the predictive capability. The term within the square brackets of (21) is thus the effective acceleration of the undisturbed flow as seen by the finite-sized particle. In an incompressible flow, the added-mass force at any time $\tilde{t}$ depends only on the undisturbed flow acceleration at that time. In a compressible flow, due to the finite propagation speed of the disturbance waves, inviscid-unsteady force at any time $\tilde{t}$ depends on the past history of undisturbed flow acceleration seen by the particle, and thus represented by the convolution integral [46,47]. The undisturbed flow acceleration seen by the particle at a previous time instant $\tilde{\xi}$ is weighted by the inviscid kernel $K_{iu}(\tilde{t}-\tilde{\xi})$. The inviscid kernel has an exact analytic expression in the zero Mach number limit

$$K_{iu}(\tilde{t}-\tilde{\xi}) = e^{(\tilde{t}-\tilde{\xi})}\cos(\tilde{t}-\tilde{\xi}). \qquad (22)$$
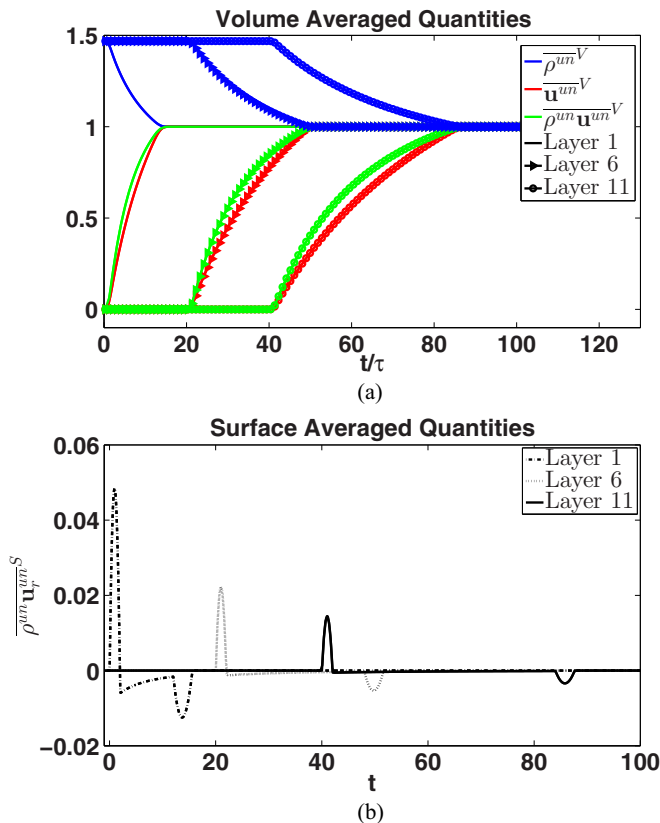
FIG. 5. Volume-averaged density, velocity, and streamwise momentum in panel (a) and surface-averaged radial momentum in panel (b) plotted as a function of acoustic time for a particle located in the first layer, sixth layer, and eleventh layer.

Here and in (19), the tilde represents time nondimensionalized with the acoustic timescale as follows: $\tilde{t} = t/\tau$, where $\tau = R/c$ and c is the speed of sound. It was observed that the above kernel is adequate for low Mach numbers (based on relative velocity between the particle and the ambient flow). So here we will simply use the above kernel without any Mach number correction.

This model, which is derived for a single particle in a compressible flow, has been rigorously tested for shock-particle interaction. The most important feature of this model is its ability to better capture the unsteady force effect. Mehta *et al.* [16] showed that in the early times of interest, the inviscid forces contributed the most to particle drag.

In the present case of an expansion wave sweeping over a particle, the various flow related quantities in (19) can be precisely calculated from the analytical solution of density and fluid velocity within the expansion wave. In Fig. 5(a), we present $\overline{\rho^{un}}^V$, $\overline{\mathbf{u}^{un}}^V$, and $\overline{\rho^{un}\mathbf{u}^{un}}^V$, and in Fig. 5(b), we present $\overline{\rho^{un}\mathbf{u}_r^{un}}^S$ plotted as a function of acoustic time, t/τ, for a particle located in the first layer, sixth layer, and eleventh layer. Note that all quantities have been scaled by the post-tail velocity and density, u_3 and ρ_3. In Fig. 5(a), $\overline{\rho^{un}}^V$, $\overline{\mathbf{u}^{un}}^V$, and $\overline{\rho^{un}\mathbf{u}^{un}}^V$ are plotted in blue, red, and green respectively. The three different particle layers are denoted by solid lines (1), triangles (6), and circles (11).

We observe that the volume-averaged density, velocity and momentum decay quickly to the post-tail values for the first particle. For particles further downstream, it takes progressively longer. In fact, the change from the prehead (PH) state to the post-tail (PT) state happens in about 15
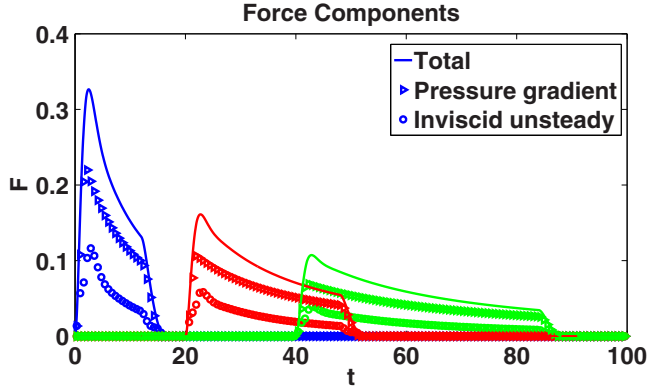
FIG. 6. The contributions of the pressure gradient term (right triangle) and the inviscid unsteady term (circle) to the total drag force experienced by particles in layers 1 (blue), 6 (red), and 11 (green).

acoustic timescales for the first particle, 30 for the sixth, and 45 for the eleventh. Thus we expect the upstream particles to have a higher drag force than the downstream particles because of the more rapid change in a shorter amount of time. The surface-averaged radial momentum for each particle sees a sharp positive spike early on, when the expansion head first sweeps over the particle. As the wave passes over the particle, the radial momentum becomes negative, gradually decreasing in magnitude before another large, negative spike when the tail of the expansion wave passes over the particle. The large negative spike occurs approximately 15, 50, and 85 acoustic time units after the expansion head initially sweeps over the respective particles. The corresponding force components $\mathbf{F}_{pg}(t)$ and $\mathbf{F}_{iu}(t)$ and the total force $\mathbf{F}$ calculated using the above flow properties are shown in Fig. 6. The forces have been nondimensionalized by the outflow conditions to give the drag coefficient, $C_D = \mathbf{F}_D / \frac{1}{2}\rho_3 u_3^2 A$, where $\mathbf{F}_D$ is the respective drag force and A is the cross-sectional area of the particles. It is evident that the pressure gradient term contributes the most to the total drag, roughly 70%. More interestingly, however, the inviscid unsteady force contributes 30% to the total particle drag force. In this type of flow configuration, neither term can be ignored. For the first particle, the total drag force peaks at approximately $t/\tau = 2.5$. The pressure gradient term reaches its peak value just before that, at $t/\tau = 2.0$, while the inviscid unsteady term achieves a peak value at $t/\tau = 2.8$. Similar behavior is observed for the other particle layers as well. It should be noted that for each particle, there exists a very short time period for which the inviscid unsteady term contributes more than the pressure gradient term. This only happens at very early and very late times (corresponding to the expansion head first hitting the particle and to the expansion tail sweeping past), when the pressure gradient force is very low.

B. Drag

Plotted in Fig. 7(a) are the fully resolved simulation results from CMT-NEK for the drag coefficient, with open faced diamonds representing $V3$ and the GF prediction with solid curves, as a function of nondimensional acoustic time, t/τ. Going from left to right, the first set of curves is the drag for a particle in the first layer (blue), the second set for a particle in the second layer (red), etc. We observe that for the first particle, the model predicts the drag extremely well. We see an excellent match in the initial slope, peak drag force at $C_D = 0.325$, and the decay. In general, the model predicts the increase in drag extremely well for the subsequent particle layers but tends to overpredict the peak force experienced by particles that are deeper in the particle array. After a particle experiences the peak force, the initial decay in drag is also captured fairly well; we begin to notice deviation from the model once the wave moves deeper into the particle bed, as seen in Fig. 7(b). The model was designed for only a single particle in a compressible flow. Where the model deviates is when the
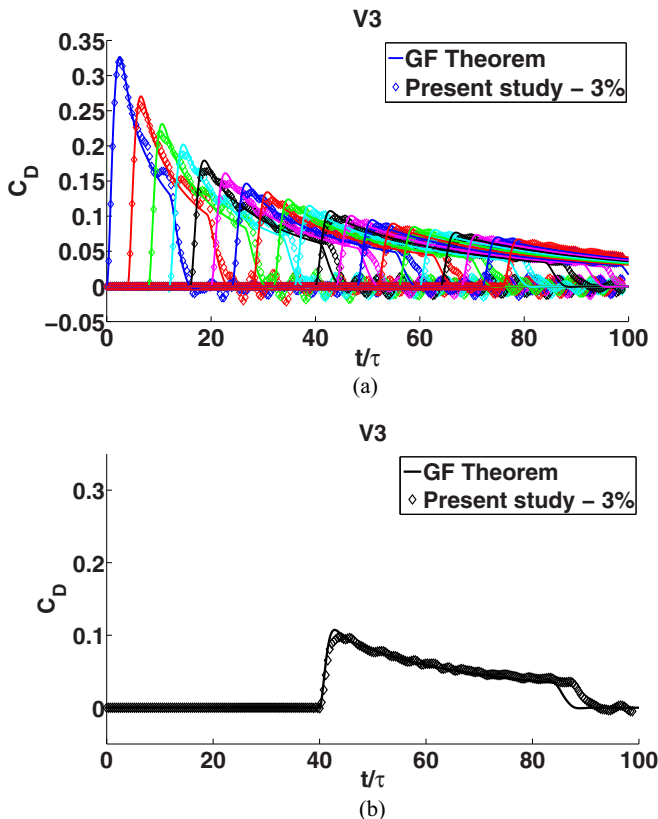
FIG. 7. (a) The drag coefficient, $C_D = F_D/\rho u^2 A$, where F_D is the drag force and A is the cross-sectional area of the particle, plotted as a function of nondimensional time t/τ, for the first 20 particle layers for our fully resolved simulation results from CMT-NEK (open symbols) for $V3$ and for the single-particle model predictions from Annamalai and Balachandar [24] (solid curves). In frame (b), we plot a particle in the eleventh layer to highlight the deviation from the model prediction.

particle begins feeling the effect of its neighbors. For every particle layer that the expansion wave encounters, multiple waves are generated. The transmitted wave is the wave that keeps propagating further downstream into the bed. The reflected wave is the wave that reflects off of the individual particles and propagates upstream as disturbances. These diffracted waves are seen as bumps in the simulation particle drag force.

In Fig. 7, the first particle's drag force is captured well until the wave reaches the second particle layer. When the transmitted wave hits the second particle layer, a reflected wave propagates back upstream. Just when the second particle layer experiences the peak drag force, we observe that the first particle layer experiences a slight increase or bump in drag which is due to a reduction in the wake pressure of the first layer. As the wave propagates to the third layer, we observe a slight increase in the drag force for layer 2 and an even greater increase for layer one. By the time the wave reaches layer 4, the drag for layer 1 has almost completely decayed. This behavior continues far downstream as the expansion wave generates more reflected waves that propagate upstream and interfere with the other particles. For the first particle layer, the decay in drag is captured very well. Further downstream, we begin to observe the dissipative effects of the particle bed.

In Fig. 8, we plot the particle drag forces for $V10$ and $V15$ in the same fashion as we did for $V3$ alongside the results from the GF theorem. In both cases, the peak force and initial slope are
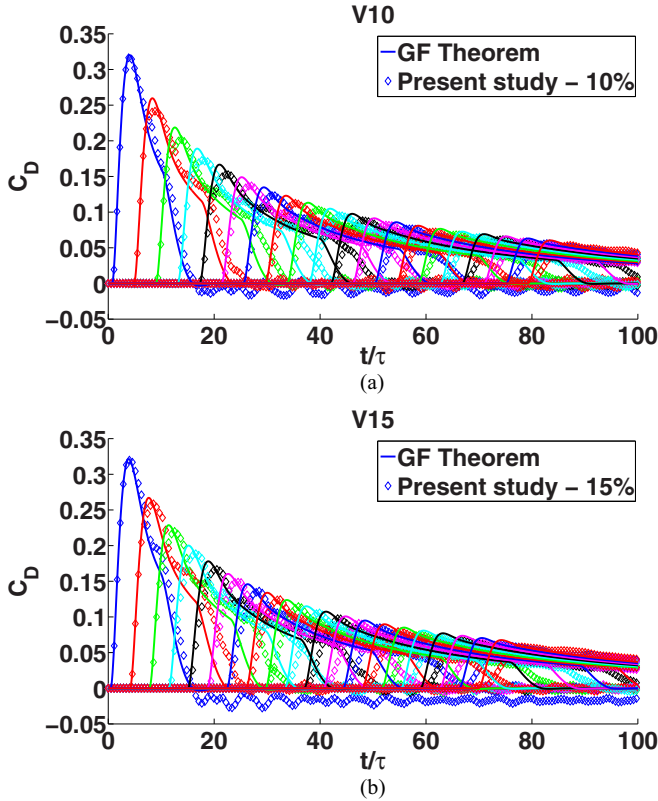
FIG. 8. The drag coefficient, $C_D = F_D / \rho u^2 A$, where F_D is the drag force and A the cross-sectional area of the particle, plotted as a function of nondimensional time t/τ, for the first 20 particle layers for our fully resolved simulation results from CMT-NEK (open symbols) for $V10$ in panel (a) and for $V15$ in panel (b). Shown with solid curves are the single particle model predictions from Annamalai and Balachandar [24].

predicted well for the first particle layer. The subsequent peak forces are slightly underpredicted but, more importantly, are slightly delayed compared to the GF model.

The particles in these two cases are significantly closer together than in $V3$ and we observe more interference with the expansion wave head, where before it was far less affected. Just like in $V3$, we observe fluctuations in drag resulting from pressure reflections from streamwise and transverse neighbors in the form of bumps in the drag coefficient. However, because of the more compact particle beds, these fluctuations in drag are slightly larger than for $V3$. In $V3$, we also observed that after the expansion tail has swept over the particles, the drag goes down to 0 and proceeds to fluctuate about this value for all particles. For $V10$ and $V15$, the same happens for every particle except the ones in the first layer, closest to the outflow. In $V10$ and especially $V15$, the drag on the first particle remains mostly negative after the tail has swept over.

C. Flow field

We now examine the instantaneous flow fields for $V3$, $V10$, and $V15$. The figures in this section are all taken as slices from the center of the particle bed. In Fig. 9, we plot contours of the gas pressure, P/P_4, inside the particle bed for $V15$ at various times, t/τ. Figure 9(b) corresponds to the time instant when the expansion wave head just passes over the first particle layer and Fig. 9(e) to the instant when the head passes over the last particle layer. In Figs. 9(b) and 9(c), the expansion head changes from a sharp front to a bowlike shape as it passes through the particle layers. The
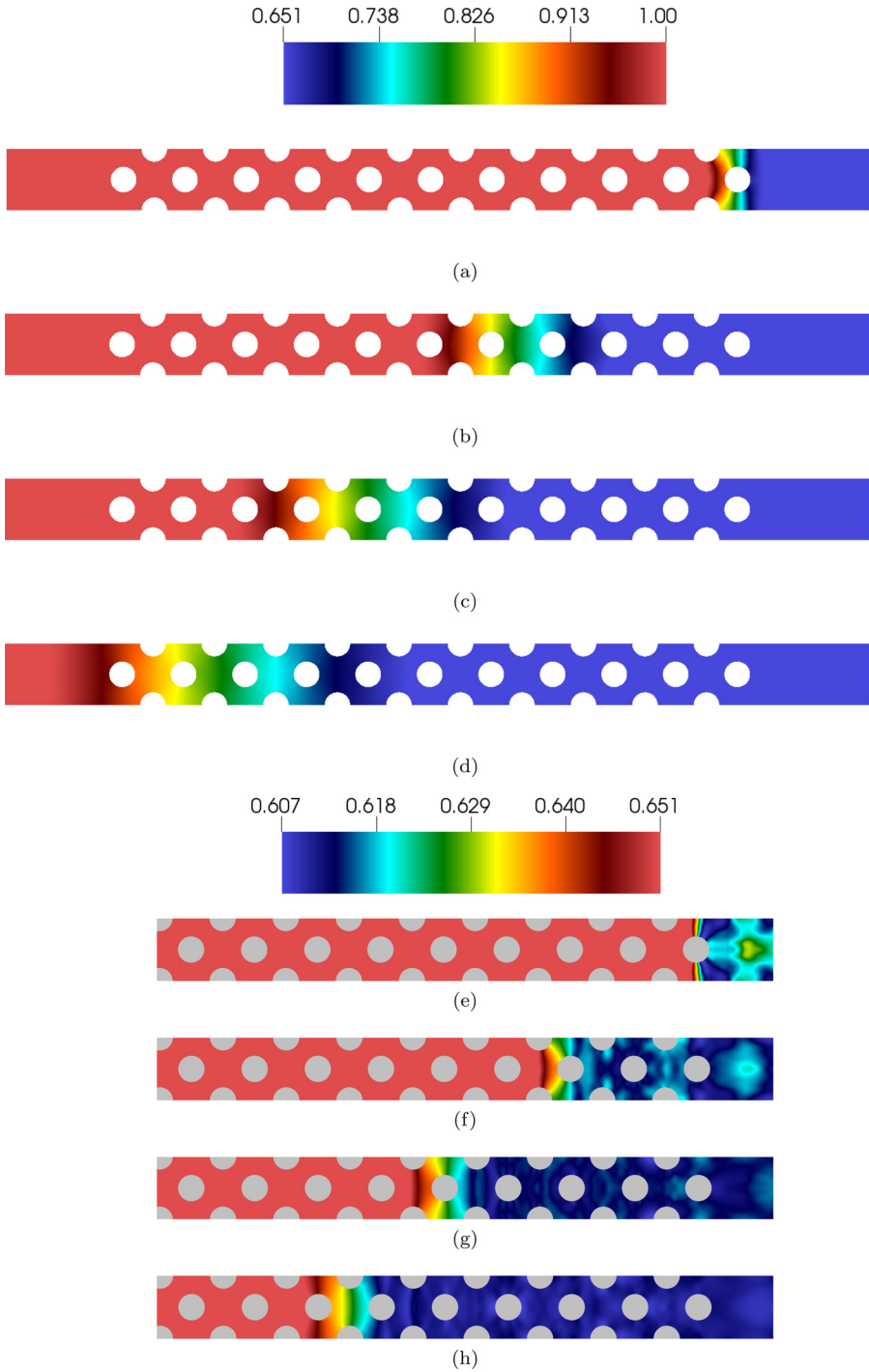
FIG. 9. Contour plots of nondimensional gas pressure, P/P_4, inside the particle bed for $V15$ at times, $t/\tau = 7,\ 41,\ 63,$ and 88, from when the expansion wave head passes over the first particle layer to when it leaves the particle bed in frames (a)–(d). In the subsequent frames, (e)–(h), we change the legend scale to better highlight the fluctuations that occur inside the bed at times $t/\tau = 10,\ 41,\ 63,$ and 88.
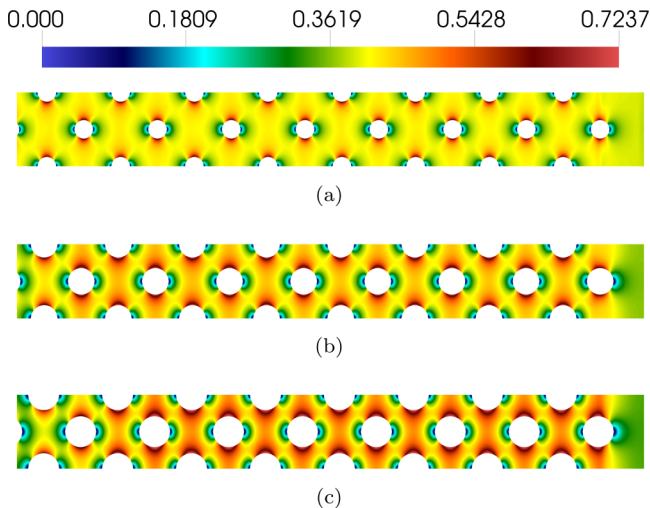
FIG. 10. Contour plots of Mach number for (a) $V3$, (b) $V10$, and (c) $V15$ at the time instance $t/\tau = 63$.

wave weakens and gets broader while it propagates further into the particle bed in Fig. 9(d). The expansion wave stretches across eight particle layers as it nears the end of the bed in Fig. 9(e). In these instances, the front, which has significantly weakened, does not have the bowlike shape seen at early times. In Figs. 9(g)–9(j), we plot the gas pressure P/P_4 at similar times but with a different scale for the contours to highlight the fluctuations that occur in the bed when the expansion wave sweeps over the particles.

We plot the contours of Mach number inside the particle beds in Figs. 10(b)–10(d) for $V3$, $V10$, and $V15$, respectively. The contours are plotted at the time instant when the expansion wave head passes over the sixteenth particle layer and exits the image frame. In all three cases, low-Mach-number regions develop on the upstream and downstream side of each particle, corresponding to the stagnation points on a sphere. High-Mach-number regions develop around the azimuthal area of the particles. The upstream particles in $V3$ experience a maximum surface Mach number of $\mathrm{Ma} = 0.678$, while $V10$ and $V15$ experience slightly higher surface Mach numbers of $\mathrm{Ma} = 0.756$ and $\mathrm{Ma} = 0.862$, respectively. In general, the higher volume fraction cases develop a higher Mach number field as the flow squeezes past the particles.

D. Mean quantities

In the following figures, we plot cross-section-averaged profiles of various quantities scaled by the high-pressure region, 4, values. The planar average is taken over a finitely sized slice at a number of streamwise points throughout the particle bed at different instances in time, starting at the time when the expansion wave head collides with the first particle layer. Throughout these figures, the time series will proceed from the right at $x = 40$, the location of the first particle layer, toward the left at $x = 0$, the location of the last particle layer. A series of five data sets is plotted for every case. Starting at the rightmost data set on every plot and proceeding to the left, time intervals of $t = 0.05$ (red), 0.2 (green), 0.35 (cyan), 0.55 (blue), and 0.7 (black) are represented.

The nondimensional cross-stream averaged gas density, $\langle \rho \rangle / \rho_4$, is plotted in Fig. 11. The gas density is initially at 1.0 and quickly decays to a value that fluctuates between 0.6 and 0.7, with a larger range of fluctuations occurring for the higher volume fraction cases, $V10$ and $V15$, and a lower range for $V3$. Between particle layers, density can vary as much as 20% of the post-tail density as the flow has to navigate around the particles. Particles deeper in the bed take progressively longer to experience the same density drop. The value of density (and other quantities) at $x = 40$ at early
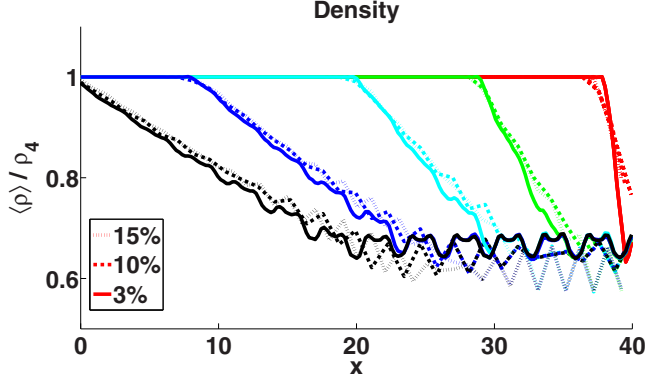
FIG. 11. Plot of nondimensional gas density as a function of depth into the bed for all three cases, solid curves representing V3, dashed curves representing V10, and dotted curves representing V15. $x = 40$ is the position of the first particle layer and $x = 0$ is that of the last particle layer. The colors represent different instances in time, increasing from right to left, starting at red, when the expansion wave head first hits the particles, proceeding to green, cyan, and blue as it propagates through the bed, and black as the head leaves the bed.

time differs between $V3$, $V10$, and $V15$. This is due to the binning procedure shown in Fig. 12(b). In plane 1, the average for $V10$ and $V15$ will be different because the expansion wave has already interacted with the particles in the first layer. On the contrary, for $V3$ in plane 1, the expansion wave has not swept over the first particle layer.

In Fig. 12(a), we show the schematic for the model we will use to predict the nondimensional pressure and temperature drop. We use an analysis similar to Han *et al.* [29], where we model the particle bed as a nozzle or area reduction for the flow from state 4 to state 4′. Rather than a continuous area reduction, we assume an instantaneous area reduction from state 4 to 4′. Using isentropic flow through a nozzle relations, for a given tail Mach number we first compute A_4/A^*, the required area ratio that would accelerate the flow from state 4 to the sonic state, denoted by the asterisk (*), as well as P_4/P^* and T_4/T^* using Eqs. (23)–(25) below:

$$\frac{A}{A^*} = \frac{1}{Ma}\left[\left(\frac{2}{\gamma+1}\right)\left(1+\frac{\gamma-1}{2}Ma^2\right)\right]^{\frac{\gamma+1}{2(\gamma-1)}}, \tag{23}$$

$$\frac{P}{P^*} = \left[\left(\frac{2}{\gamma+1}\right)\left(1+\frac{\gamma-1}{2}Ma^2\right)\right]^{-\frac{\gamma}{\gamma-1}}, \tag{24}$$

$$\frac{T}{T^*} = \left[\left(\frac{2}{\gamma+1}\right)\left(1+\frac{\gamma-1}{2}Ma^2\right)\right]^{-1}. \tag{25}$$

The effective area reduction, or $A_{4'}/A_4$, is 0.97, 0.9, and 0.85 respectively for $V3$, $V10$, and $V15$. Now knowing A_4/A^* and $A_{4'}/A_4$, we can easily compute $A_{4'}/A^*$. From this area ratio, we can readily obtain $Ma_{4'}$ and hence $P_{4'}/P^*$ and $T_{4'}/T^*$. Using the initial values P_4 and T_4, we can set up a chain of ratios to obtain the final pressures and temperatures as

$$T_{4'} = \frac{T_{4'}}{T^*}\frac{T^*}{T_4}T_4, \tag{26}$$

and

$$P_{4'} = \frac{P_{4'}}{P^*}\frac{P^*}{P_4}P_4. \tag{27}$$
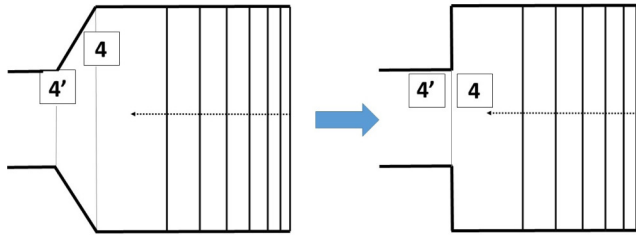
(a)
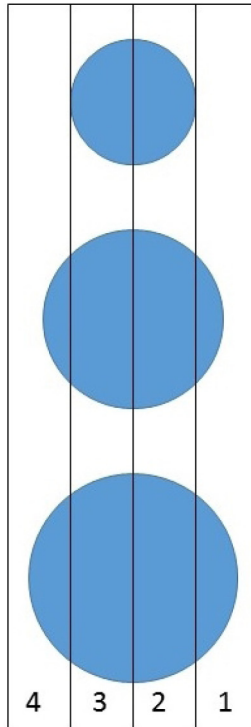
(b)

FIG. 12. An isentropic flow model is utilized by assuming that the particle bed acts similar to a converging nozzle. The main assumption in panel (a) is that the area change from state 4 to state 4′ occurs instantaneously at every particle layer. A schematic of the planar-averaged binning procedure is shown in panel (b).

As we will see, this simple analysis gives very good predictions for final pressure, temperature, and Mach number.

In Figs. 13 and 14, we plot the averages of gas pressure and gas temperature (symbols), respectively, throughout the particle bed and the analytical results (solid lines). The pressure and temperature have been scaled by the high-pression-region values, P_4 and T_4 respectively.

Nondimensional pressure and temperature behave similarly to density as the expansion propagates through the bed. The pressure and temperature inside the particle bed have prehead values $\langle P \rangle / P_4 = 1.0$ and $\langle T \rangle / T_4 = 1.0$ respectively. As the expansion propagates into the bed, the first layer of particles see a very sudden attenuation. Particles further downstream see a much more gradual drop. We note that the wave in case $V3$ moves more rapidly through the bed as opposed to $V10$ and $V15$, as indicated by the faster pressure and temperature drops. Further, as the tail sweeps over the particle bed, the gas pressure and gas temperature settle at slightly different post-tail
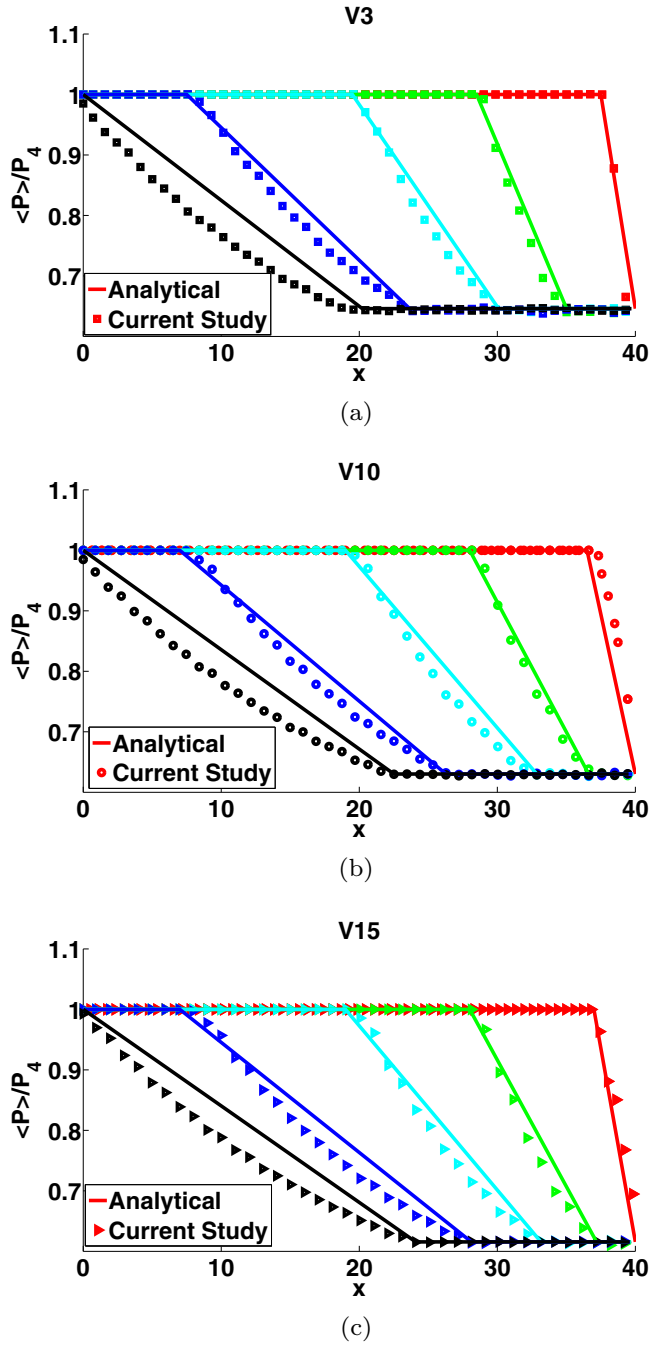
FIG. 13. Plot of nondimensional gas pressure as a function of depth into the bed for cases (a) V3 (squares), (b) V10 (circles), and (c) V15 (right triangles). The analytical solution is shown in solid lines. $x = 40$ is the position of the first particle layer and $x = 0$ is that of the last particle layer. The colors represent different instances in time, increasing from right to left, starting at red, when the expansion wave head first hits the particles, proceeding to green, cyan, and blue as it propagates through the bed, and black as the head leaves the bed.
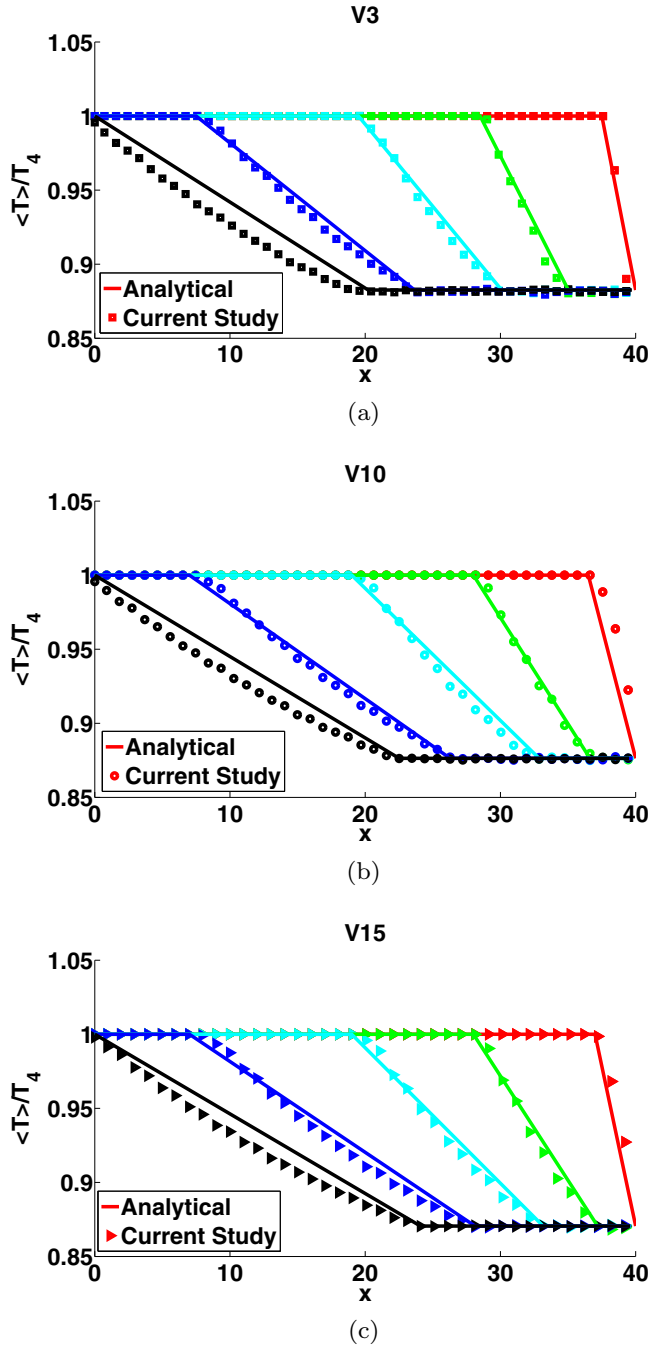
FIG. 14. Plot of nondimensional gas temperature as a function of depth into the bed for cases (a) V3 (squares), (b) V10 (circles), and (c) V15 (right triangles). The analytical solution is shown in solid lines. $x = 40$ is the position of the first particle layer and $x = 0$ is that of the last particle layer. The colors represent different instances in time, increasing from right to left, starting at red, when the expansion wave head first hits the particles, proceeding to green, cyan, and blue as it propagates through the bed, and black as the head leaves the bed.

Mach number

(a)

(b)
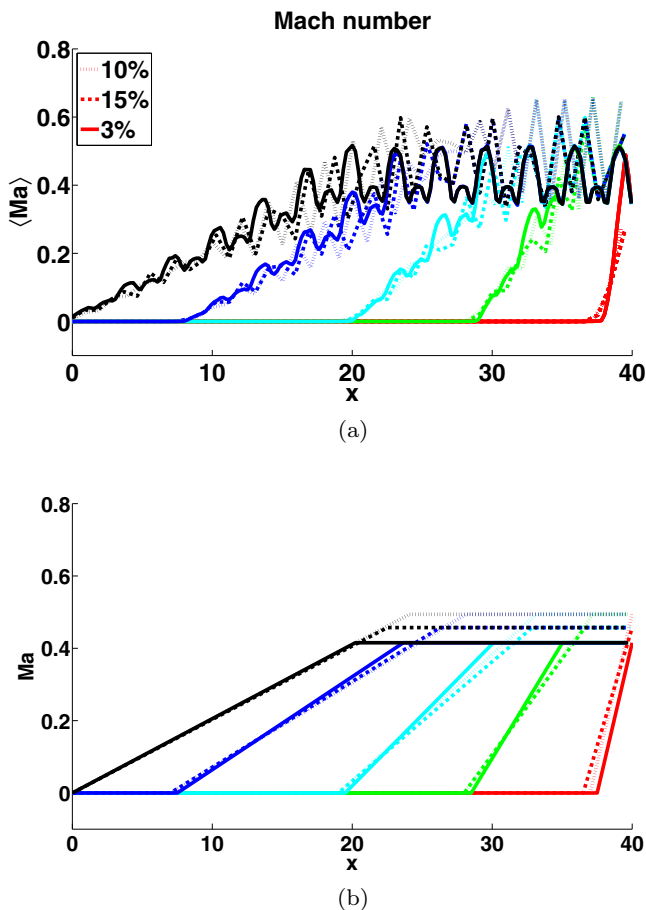
FIG. 15. Plot of Mach number as a function of depth into the bed for all three cases in panel (a), solid lines representing V3, dashed curves representing V10, and dotted curves representing V15. $x = 40$ is the position of the first particle layer and $x = 0$ is that of the last particle layer. The colors represent different instances in time, increasing from right to left, starting at red, when the expansion wave head first hits the particles, proceeding to green, cyan, and blue as it propagates through the bed, and black as the head leaves the bed. Frame (b) shows the analytical results from an isentropic flow through an area change analysis.

values. $V3$ sees final post-tail pressure and temperature of $\langle P \rangle / P_{4'} = 0.644$ and $\langle T \rangle / T_{4'} = 0.882$, while $V10$ sees final values of $\langle P \rangle / P_{4'} = 0.630$ and $\langle T \rangle / T_{4'} = 0.876$, and lastly $V15$ sees values of $\langle P \rangle / P_{4'} = 0.616$ and $\langle T \rangle / T_{4'} = 0.870$. This compares very well to the isentropic flow results, with final pressures and temperatures of $\langle P \rangle / P_{4'} = 0.646$, $\langle T \rangle / T_{4'} = 0.883$ for $V3$, $\langle P \rangle / P_{4'} = 0.630$, $\langle T \rangle / T_{4'} = 0.876$ for $V10$, and $\langle P \rangle / P_{4'} = 0.616$, $\langle T \rangle / T_{4'} = 0.871$ for $V15$. However, we do observe some discrepancy in the intermediate state between initial and final pressures and temperatures. Whereas the analytical results have a linear slope, the simulation results have a more parabolic shape. There are several reasons for these discrepancies. For one, the isentropic flow relations assume a continuous area change from state 4 to state $4'$. This is why we observe intense fluctuations throughout the bed in the simulations. Further, the particles act to produce wave reflections that emanate back upstream and interfere with the flow, which the simple isentropic flow through an area change analysis does not take into account.

In Fig. 15, we plot the planar-averaged local Mach number as a function of depth into the particle bed from the present simulation [Fig. 15(a)] and for the analytical results from the isentropic flow
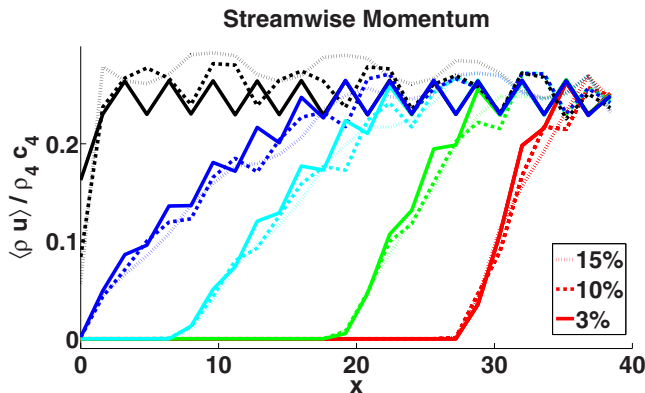
FIG. 16. Plot of the nondimensional streamwise momentum as a function of depth into the bed for all three cases, solid lines representing V3, dashed curves representing V10 and dotted curves representing V15. The quantities have been nondimensionalized by $\rho_4 c_4^2$. $x = 40$ is the position of the first particle layer and $x = 0$ of the last particle layer. The colors represent different instances in time, increasing from right to left, starting at red, when the expansion wave head first hits the particles and proceeding to green, cyan, and blue as it propagates through the bed.

analysis [Fig. 15(b)]. The speed of sound used for the Mach number is the value in the high-pressure region, c_4. The particle bed acts like a sudden contraction when the expansion wave first hits the bed. This area change results in a nozzling of the flow as it accelerates and navigates around the particles. As the wave propagates through the different particle layers, it encounters many such converging and diverging sections. This is evident in Fig. 15 as the planar averaged local Mach number fluctuates between the particle layers. Initially, the particle bed sees no flow; as the expansion head propagates into the bed, the flow accelerates rapidly. Because of the converging-diverging effect of the particle layers, the particle bed Mach number fluctuates between values of 0.34 and 0.65 for the three cases, tending to a wider range for higher volume fractions. The average particle bed Mach numbers, $Ma_{4'}$, are 0.43, 0.46, and 0.49 for $V3$, $V10$, and $V15$ respectively. The particles themselves, however, experience a much higher surface Mach number, with peak values of 0.678, 0.756, and 0.862 respectively for the three cases. The analytical results in Fig. 15(b) show good agreement with the simulation results, with average particle bed Mach numbers of 0.42, 0.46, and 0.49. As before with pressure and temperature, the slope of the intermediate region is linear for the analytical results, whereas it fluctuates significantly for the simulation results. Further, there are much more intense fluctuations in the Mach number than for the pressure and temperature and this is much more readily apparent when compared to the analytical result.

E. Conserved quantities

We plot the nondimensional streamwise momentum, $\langle \rho u \rangle / \rho_4 c_4$, and the nondimensional streamwise kinetic energy, $\langle \rho u^2 \rangle / \rho_4 c_4^2$, in Figs. 16 and 17, respectively. We observe a trend similar to that with the Mach number. While the average conserved streamwise momentum is approximately the same for all three cases at $\langle \rho u \rangle / \rho_4 c_4 = 0.27$, the average streamwise kinetic energy varied from $\langle \rho u^2 \rangle / \rho_4 c_4^2 = 0.125$ for $V3$ to $\langle \rho u^2 \rangle / \rho_4 c_4^2 = 0.143$ for $V10$ and $V15$. The streamwise kinetic energy fluctuates much more intensely inside the bed than the streamwise momentum. In general, the higher volume fractions experience the greatest fluctuations, with cases $V10$ and $V15$ having fluctuations on the order of 50% of the average post-tail values.

In Fig. 18, we plot the nondimensional conserved plane averaged total specific energy of the particle bed, $\langle \rho E \rangle / \rho_4 c_4^2$. Initially, the bed is at a prehead value of $\langle \rho E \rangle / \rho_4 c_4^2 = 1.79$ for all three cases and quickly decays once the expansion wave head hits the first layer of particles. At later time,

Streamwise Kinetic Energy
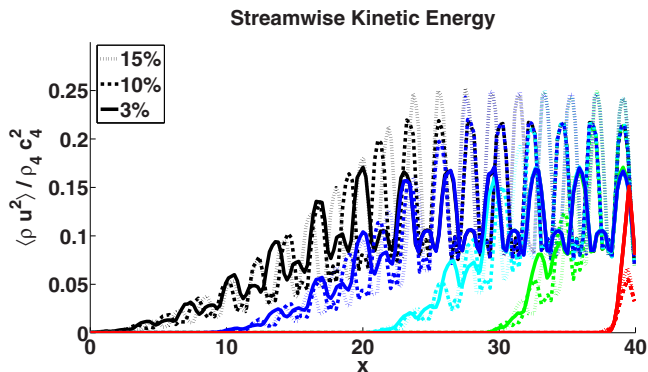
FIG. 17. Plot of the nondimensional streamwise kinetic energy as a function of depth into the bed for all three cases, solid lines representing V3, dashed curves representing V10, and dotted curves representing V15. $x = 40$ is the position of the first particle layer and $x = 0$ is that of the last particle layer. The colors represent different instances in time, increasing from right to left, starting at red, when the expansion wave head first hits the particles, proceeding to green, cyan, and blue as it propagates through the bed, and black as the head leaves the bed.

indicated by the bottom left most curves, the total energy decays to post-tail values of $\langle \rho E \rangle / \rho_4 c_4^2 = 1.07$, $\langle \rho E \rangle / \rho_4 c_4^2 = 1.04$, and $\langle \rho E \rangle / \rho_4 c_4^2 = 1.02$, respectively for $V3$, $V10$, and $V15$. This shows that the denser packed particles dissipate more energy as the wave propagates through the bed. As before, the wave travels faster through $V3$ than the other two cases as can be observed by the more rapid dissipation in total energy.

F. Fluctuating quantities

As was apparent in the previous figures, there are significant fluctuations about mean values happening throughout the bed as the particles act like converging-diverging nozzles for the flow to

Total Specific Energy
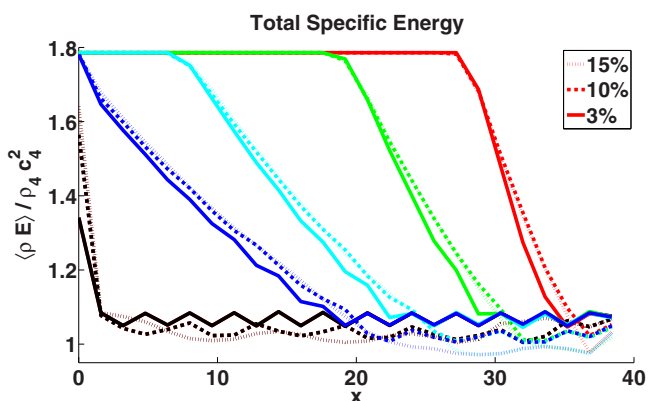
FIG. 18. Plot of the nondimensional conserved total specific energy as a function of depth into the bed for all three cases, solid lines representing V3, dashed curves representing V10, and dotted curves representing V15. $x = 40$ is the position of the first particle layer and $x = 0$ is that of the last particle layer. The colors represent different instances in time, increasing from right to left. Starting at red, when the expansion wave head first hits the particles, proceeding to green, cyan, and blue as it propagates through the bed, and black as the head leaves the bed.
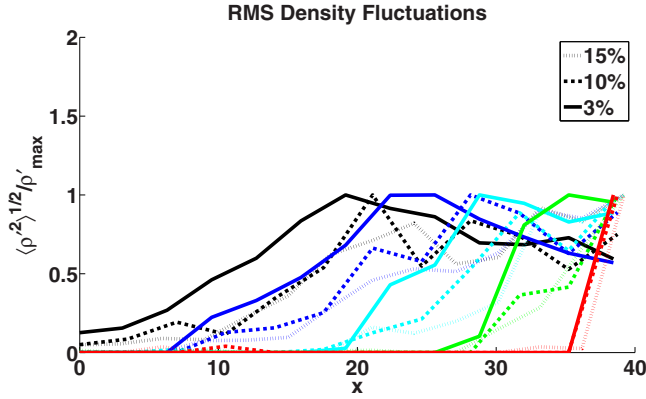
FIG. 19. Plot of the nondimensional root-mean-square (rms) density fluctuations normalized by the maximum density fluctuation at each time as a function of depth into the bed for all three cases, solid lines representing V3, dashed curves representing V10, and dotted curves representing V15. $x = 40$ is the position of the first particle layer and $x = 0$ is that of the last particle layer. The colors represent different instances in time, increasing from right to left. Starting at red, when the expansion wave head first hits the particles and proceeding to green, cyan, and blue as it propagates through the bed.

navigate through. In the following figures, we examine the root-mean-square (rms) fluctuations of our state variables and velocity. In Fig. 19, we plot the planar-averaged rms density fluctuations, scaled by the maximum density fluctuations at each time interval. The density fluctuations peak immediately upon arrival of the expansion wave. In general, for all cases, the peak fluctuations are stronger and occur more frequently at early times.

The nondimensional rms streamwise velocity fluctuations scaled by the maximum value at each time interval are presented in Fig. 20 as a function of space and time. The rms velocity behaves similar to the rms density. There is a very rapid increase early on, with the most intense fluctuations
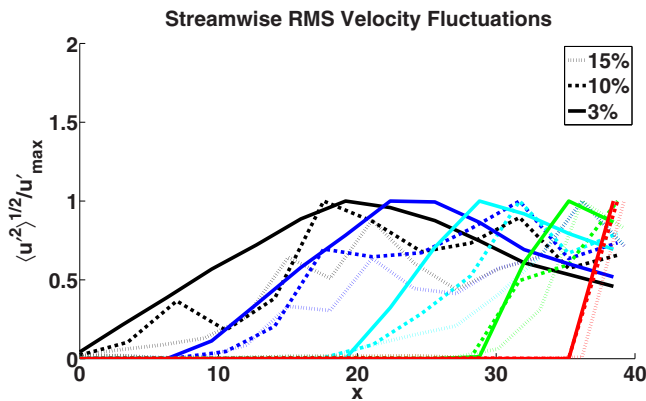
FIG. 20. Plot of the nondimensional rms streamwise velocity fluctuations normalized by the maximum velocity fluctuation at each time as a function of depth into the bed for all three cases, solid lines representing V3, dashed curves representing V10, and dotted curves representing V15. $x = 40$ is the position of the first particle layer and $x = 0$ is that of the last particle layer. The colors represent different instances in time, increasing from right to left. Starting at red, when the expansion wave head first hits the particles, proceeding to green, cyan, and blue as it propagates through the bed, and black as the head leaves the bed.

RMS Pressure Fluctuations
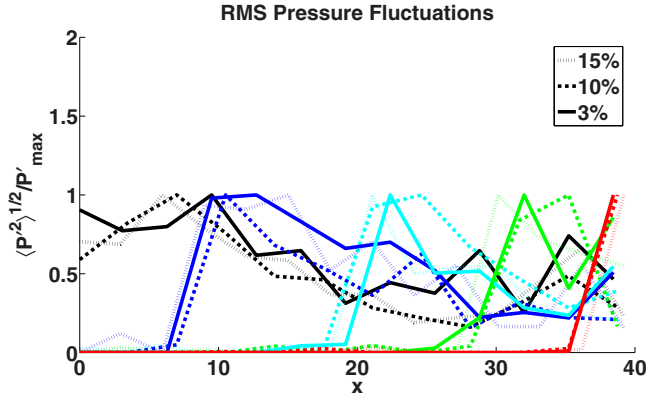
FIG. 21. Plot of the nondimensional rms pressure fluctuations normalized by initial pressure as a function of depth into the bed for all three cases, solid lines representing V3, dashed curves representing V10, and dotted curves representing V15. $x = 40$ is the position of the first particle layer and $x = 0$ is that of the last particle layer. The colors represent different instances in time, increasing from right to left. Starting at red, when the expansion wave head first hits the particles, proceeding to green, cyan, and blue as it propagates through the bed, and black as the head leaves the bed.

occurring at early times. $V3$ has higher, more frequent peak density, and velocity fluctuations at later times than $V10$ and $V15$.

We plot the planar-averaged nondimensional rms pressure and temperature fluctuations scaled by the peak fluctuating values as functions of space in Figs. 21 and 22. The peak pressure fluctuations occur pretty regularly throughout the bed. $V3$ experiences the lowest peak fluctuations for temperature and pressure, on average equal to 0.4. $V10$ and $V15$ on average have fluctuations of 80% of the peak throughout the bed. One reason for this might be the confining effect of the higher volume fraction cases. The larger particles create greater wakes and unsteadiness.

RMS Temperature Fluctuations
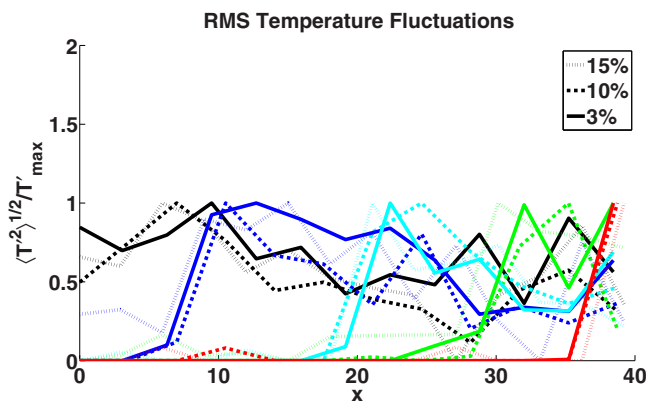
FIG. 22. Plot of nondimensional rms temperature fluctuations normalized by initial temperature as a function of depth into the bed for all three cases, solid lines representing V3, dashed curves representing V10, and dotted curves representing V15. $x = 40$ is the position of the first particle layer and $x = 0$ is that of the last particle layer. The colors represent different instances in time, increasing from right to left. Starting at red, when the expansion wave head first hits the particles, and proceeding to green, cyan, and blue as it propagates through the bed.

The nondimensional rms temperature fluctuations, in Fig. 22, behave similarly to the aforementioned pressure fluctuations. We see the highest peaks for $V10$ and $V15$ throughout the bed. $V3$ has comparable peak fluctuations as $V10$ and $V15$ at early times only. The total pressure drop in the bed is also greater than the total temperature drop, so the magnitude of the pressure fluctuations is also larger.

IV. CONCLUSION

Using CMT-NEK, a discontinuous Galerkin spectral element flow solver, we simulated three cases of an expansion wave propagating into a face-centered cubic array of particles. The three cases considered have volume fractions of 3%, 10%, and 15%. We examined pressure, temperature, density, and Mach number changes throughout the particle bed at varying times and compared these results to theory obtained from a simple isentropic flow through a nozzle. The analytical results compared well for the post-tail states of pressure, temperature, and Mach number; however. the most significant discrepancy occurred in the intermediate region between the head and the tail, where unsteady effects are prevalent. The model assumes a linear area change, whereas in the simulations we have a nonlinear area change due to the converging-diverging nozzle effect of the particles arrays. The root-mean-square fluctuations of various quantities were also examined. The 3% volume fraction case has much higher fluctuations in density and velocity than the 10% and 15% volume fraction cases. On the other hand, 10% and 15% have higher fluctuations in temperature and pressure.

Though the particles were stationary in this study, it is important to understand the drag, which causes particle motion, that the particle bed experiences. We note that the inviscid drag models of Annamalai and Balachandar [24] for a single particle in compressible flows showed very good agreement with the drag experienced by the first particle layer. Deviation from the model occurred as the wave propagated further into the bed and interactions with neighboring particles and volume fraction effects became important. The model was designed for a single particle and hence does not capture all of the complex physics in a particle bed, such as wave diffraction off of neighboring particles. These wave reflections can act to modulate or attenuate the drag in time. Future study should be performed for stronger waves generated with higher pressure ratios as well as larger volume fractions. Densely packed beds experiencing a stronger expansion wave will exhibit some interesting flow physics as the local flow reaches sonic and supersonic speeds, such as formations of shocklets that can act to dissipate energy much more intensely.

[1] E. F. Blick, High-speed flow through porous media, Ph.D. thesis, University of Oklahoma, Norman, Oklahoma, 1963 (unpublished).

[2] B. Cagnoli, A. Barmin, O. Melnik, and R. S. J. Sparks, Depressurization of fine powders in a shock tube and dynamics of fragmented magma in volcanic conduits, Earth Planet. Sci. Lett. **204**, 101 (2002).

[3] O. Igra and K. Takayama, Shock tube study of the drag coefficient of a sphere in a non-stationary flow, Proc. Royal Soc. London A **442**, 231 (1993).

[4] A. Britan, T. Elperin, O. Igra, and J. P. Jiang, Acceleration of a sphere behind planar shock waves, Exp. Fluids **20**, 84 (1995).

[5] H. Tanno, K. Itoh, T. Saito, A. Abe, and K. Takayama, Interaction of a shock with a sphere suspended in a vertical shock tube, Shock Waves **13**, 191 (2003).

[6] M. Sun, T. Saito, K. Takayama, and H. Tanno, Unsteady drag on a sphere by shock wave loading, Shock Waves **14**, 3 (2005).

[7] A. A. Martinez, G. C. Orlicz, and K. P. Prestridge, A new experiment to measure shocked particle drag using multipulse particle image velocimetry and particle tracking, Exp. Fluids **56**, 1854 (2015).

[8] A. D. Bordoloi, A. A. Martinez, and K. Prestridge, Relaxation drag history of shock accelerated microparticles, J. Fluid Mech. **823** (2017).

[9] M. Parmar, A. Haselbacher, and S. Balachandar, Modeling of the unsteady force for shock–particle interaction, Shock Waves **19**, 317 (2009).

[10] T. J. B. Collins, A. Poludnenko, A. Cunningham, and A. Frank, Shock propagation in deuterium-tritium-saturated foam, Phys. Plasmas **12**, 062705 (2005).

[11] C. Lu, S. Sambasivan, A. Kapahi, and H. S. Udaykumar, Multi-scale modeling of shock interaction with a cloud of particles using an artificial neural network for model representation, Proc. IUTAM **3**, 25 (2012).

[12] Z. Hosseinzadeh-Nik, S. Subramaniam, and J. D. Regele, Investigation and quantification of flow unsteadiness in shock-particle cloud interaction, Int. J. Multiphase Flow **101**, 186 (2018).

[13] J. D. Regele, J. Rabinovitch, T. Colonius, and G. Blanquart, Unsteady effects in dense, high speed, particle laden flows, Int. J. Multiphase Flow **61**, 1 (2014).

[14] P. Sridharan, T. L. Jackson, J. Zhang, and S. Balachandar, Shock interaction with one-dimensional array of particles in air, J. Appl. Phys. **117**, 075902 (2015).

[15] Y. Mehta, T. L. Jackson, J. Zhang, and S. Balachandar, Numerical investigation of shock interaction with one-dimensional transverse array of particles in air, J. Appl. Phys. **119**, 104901 (2016).

[16] Y. Mehta, C. Neal, T. L. Jackson, S. Balachandar, and S. Thakur, Shock interaction with three-dimensional face centered cubic array of particles, Phys. Rev. Fluids **1**, 054202 (2016).

[17] Y. Mehta, C. Neal, K. Salari, T. L. Jackson, J. Zhang, S. Balachandar, and S. Thakur, Propagation of a strong shock over a random bed of spherical particles, J. Fluid Mech. **839**, 157 (2018).

[18] J. L. Wagner, S. J. Beresh, S. P. Kearney, W. M. Trott, J. N. Castaneda, B. O. Pruett, and M. R. Baer, A multiphase shock tube for shock wave interactions with dense particle fields, Exp. Fluids **52**, 1507 (2012).

[19] J. L. Wagner, S. P. Kearney, S. J. Beresh, E. P. DeMauro, and B. O. Pruett, Flash x-ray measurements on the shock-induced dispersal of a dense particle curtain, Exp. Fluids **56**, 213 (2015).

[20] Y. Ling, J. L. Wagner, S. J. Beresh, S. P. Kearney, and S. Balachandar, Interaction of a planar shock wave with a dense particle curtain: Modeling and experiments, Phys. Fluids **24**, 113301 (2012).

[21] T. G. Theofanous, V. Mitkin, and C.-H. Chang, The dynamics of dense particle clouds subjected to shock waves. Part 1. Experiments and scaling laws, J. Fluid Mech. **792**, 658 (2016).

[22] J. A. McFarland, W. J. Black, J. Dahal, and B. E. Morgan, Computational study of the shock driven instability of a multiphase particle-gas system, Phys. Fluids **28**, 024105 (2016).

[23] E. P. DeMauro, J. L. Wagner, S. J. Beresh, and P. A. Farias, Unsteady drag following shock wave impingement on a dense particle curtain measured using pulse-burst PIV, Phys. Rev. Fluids **2**, 064301 (2017).

[24] S. Annamalai and S. Balachandar, Faxén form of time-domain force on a sphere in unsteady spatially varying viscous compressible flows, J. Fluid Mech. **816**, 381 (2017).

[25] K. Chojnicki, A. B. Clarke, and J. C. Phillips, A shock-tube investigation of the dynamics of gas-particle mixtures: Implications for explosive volcanic eruptions, Geophys. Res. Lett. **33**, L15309 (2006).

[26] V. Cigala, U. Kueppers, J. J. Peña Fernández, J. Taddeucci, J. Sesterhenn, and D. B. Dingwell, The dynamics of volcanic jets: Temporal evolution of particles exit velocity from shock-tube experiments, J. Geophys. Res.: Solid Earth **122**, 6031 (2017).

[27] P. G. Lefloch and M. D. Thanh, The Riemann problem for fluid flows in a nozzle with discontinuous cross-section, Commun. Math. Sci. **1**, 763 (2003).

[28] D. Kröner and M. D. Thanh, Numerical solutions to compressible flows in a nozzle with variable cross section, SIAM J. Numer. Anal. **43**, 796 (2005).

[29] E. E Han, M. Hantke, and G. Warnecke, Exact Riemann solutions to compressible euler equations in ducts with discontinuous cross-section, J. Hyperbolic Differential Eq. **9**, 403 (2012).

[30] E. F. Toro, *Riemann Solvers and Numerical Methods for Fluid Dynamics: A Practical Introduction* (Springer Science & Business Media, Berlin, 2013).

[31] P. F. Fischer, J. Lottes, S. Kerkemeier, K. Heisey, A. Obabko, O. Marin, and E. Merzari, http://nek5000.mcs.anl.gov.

[32] J. S. Hesthaven and T. Warburton, *Nodal Discontinuous Galerkin Methods: Algorithms, Analysis, and Applications* (Springer, New York, 2008).

[33] C. Canuto, M. Y. Hussaini, A. Quarteroni, and T. A. Zang, *Spectral Methods II: Evolution to Complex Geometries and Applications to Fluid Dynamics* (Springer-Verlag, New York, 2007).

[34] F. Hindenlang, G. J. Gassner, C. Altmann, A. Beck, M. Staudenmaier, and C. Munz, Explicit discontinuous Galerkin methods for unsteady problems, Comp. Fluids **61**, 86 (2012).

[35] L. T. Diosady and S. M. Murman, Higher-order methods for compressible turbulent flows using entropy variables, in *Proceedings of the 53rd AIAA Aerospace Science Meeting* (AIAA, Kissimmee, FL, 2015), p. 0294.

[36] D. A. Kopriva and G. J. Gassner, On the quadrature and weak form choices in collocation type discontinuous Galerkin spectral element methods, J. Sci. Comput. **44**, 136 (2010).

[37] C. Canuto, M. Y. Hussaini, A. Quarteroni, and T. A. Zang, *Spectral Methods I: Fundamentals in Single Domains* (Springer-Verlag, New York, 2006).

[38] M. O. Deville, P. F. Fischer, and E. H. Mund, *High-Order Methods for Incompressible Fluid Flow* (Cambridge University Press, Cambridge, UK, 2002).

[39] R. M. Kirby and G. E. Karniadakis, De-aliasing on non-uniform grids: Algorithms and applications, J. Comput. Phys. **191**, 249 (2003).

[40] M. S. Liou, A sequel to AUSM: AUSM+, J. Comput. Phys. **129**, 362 (1996).

[41] S. Gottlieb and C.-W. Shu, Total variation-diminishing Runge-Kutta schemes, Math. Comp. **67**, 73 (1998).

[42] J. F. Hackl, M. S. Shringarpure, R. B. Koneru, M.-O. Delchini, and S. Balachandar, A shock capturing discontinuous Galerkin spectral element method for curved geometry using entropy viscosity, Comput. Fluids (accepted).

[43] R. Hartmann and P. Houston, Symmetric interior penalty DG methods for the compressible Navier-Stokes equations I: Method formulation, Int. J. Numer. Anal. Mod. **3**, 1 (2006).

[44] V. Dolejší and M. Feistauer, *Discontinuous Galerkin Method: Analysis and Applications to Compressible Flow* (Springer, Berlin, 2015).

[45] D. Belk, D. L. Whitfield, and J. M. Janus, Three-dimensional unsteady euler equations solution on dynamic grids, AIAA J. **25**, 1160 (1987).

[46] M. Parmar, A. Haselbacher, and S. Balachandar, Generalized Basset-Boussinesq-Oseen Equation for Unsteady Forces on a Sphere in a Compressible Flow, Phys. Rev. Lett. **106**, 084501 (2011).

[47] M. Parmar, S. Balachandar, and A. Haselbacher, Equation of motion for a drop or bubble in viscous compressible flows, Phys. Fluids **24**, 056103 (2012).